Volume 15
Number 15
21 April 2023
Pages 6869-7188

Nanoscale

rsc.li/nanoscale

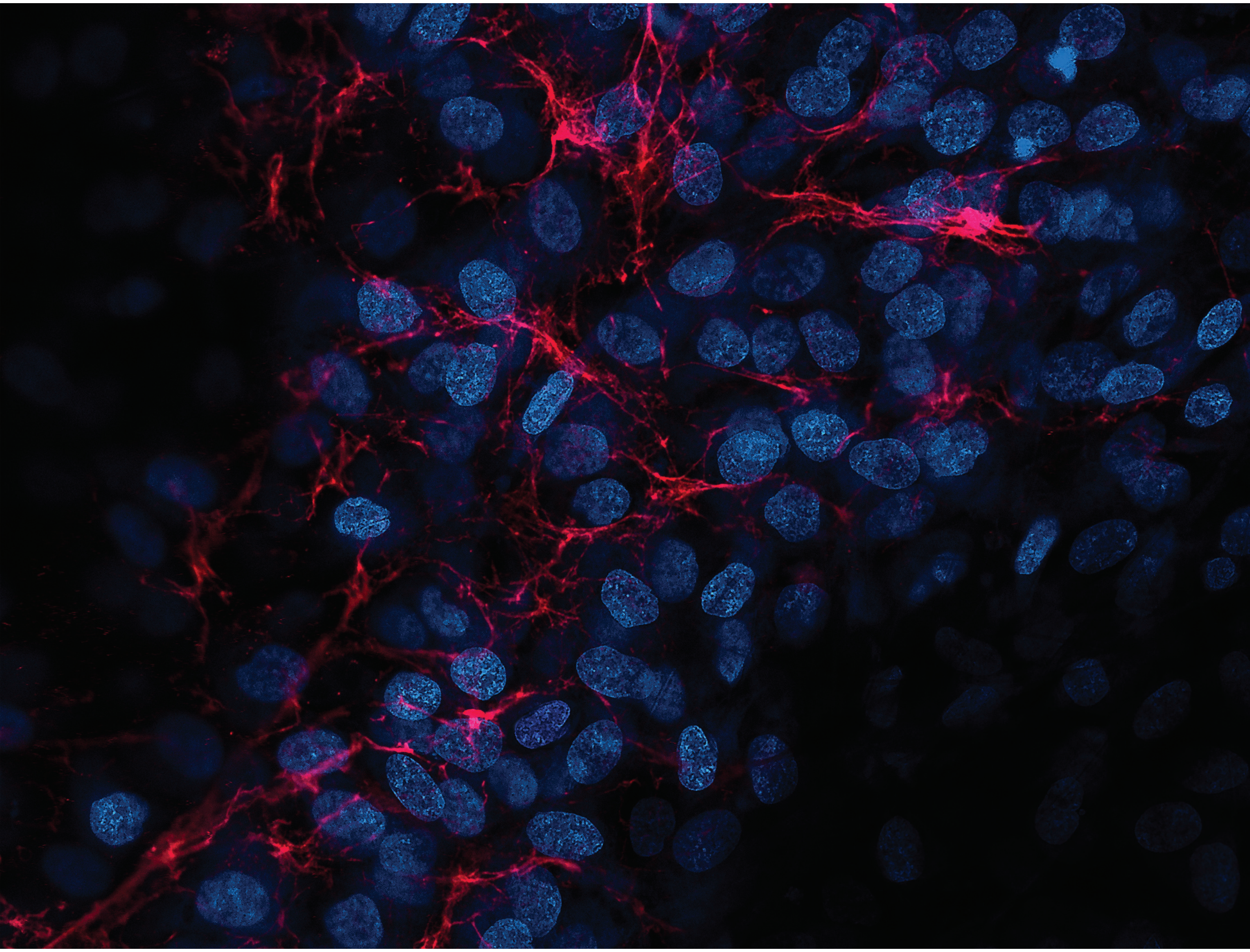

ISSN 2040-3372

ROYAL SOCIETY
OF **CHEMISTRY**

PAPER
Urszula Stachewicz *et al.*
Mimicking natural electrical environment with cellulose acetate scaffolds enhances collagen formation of osteoblasts

NCNST

Nanoscale

PAPER

View Article Online
View Journal | View Issue

Check for updates

Cite this: *Nanoscale*, 2023, **15**, 6890

Mimicking natural electrical environment with cellulose acetate scaffolds enhances collagen formation of osteoblasts†

Piotr K. Szewczyk,[a] Krzysztof Berniak,[a] Joanna Knapczyk-Korczak,[a] Joanna E. Karbowniczek,[a] Mateusz M. Marzec,[b] Andrzej Bernasik[b,c] and Urszula Stachewicz*[a]

Received 2nd January 2023,
Accepted 3rd February 2023

DOI: 10.1039/d3nr00014a

rsc.li/nanoscale

The medical field is continuously seeking new solutions and materials, where cellulose materials due to their high biocompatibility have great potential. Here we investigate the applicability of cellulose acetate (CA) electrospun fibers for bone tissue regeneration. For the first time we show the piezoelectric properties of electrospun CA fibers *via* high voltage switching spectroscopy piezoresponse force microscopy (HVSS-PFM) tests, which are followed by surface potential studies using Kelvin probe force microscopy (KPFM) and zeta potential measurements. Piezoelectric coefficient for CA fibers of 6.68 ± 1.70 pmV^{-1} along with high surface (718 mV) and zeta (−12.2 mV) potentials allowed us to mimic natural electrical environment favoring bone cell attachment and growth. Importantly, the synergy between increased surface potential and highly developed structure of the fibrous scaffold led to the formation of a vast 3D network of collagen produced by osteoblasts only after 7 days of *in vitro* culture. We clearly show the advantages of CA scaffolds as a bone replacement material, when long-lasting structural support is needed.

1. Introduction

Polymeric biomaterials can be found in almost all aspects of medicine and are rising in popularity, especially polysaccharide or protein-based, including collagen, elastin, gelatin, silk, chitosan, alginates, hyaluronic acid, and cellulose.[1,2] Their applications range from pacemakers through stitches, patches, lenses and drug-release systems to tissue scaffolds.[3–8] Cellulose and its derivatives have been researched in detail due to their biocompatibility, biodegradability, low cost and accessibility.[9–12] Cellulose has many adjustable chemical, physical and mechanical properties, making it an ideal candidate for tissue engineering.[13–15] It can be obtained from a range of natural materials, the most common being the cell wall of plants. However, bacterial cellulose has also been reported.[16,17] Being the most common biopolymer on earth, its supply is considered to be unlimited, with over 28 billion tons produced annually.[9] Cellulose, primarily used in its acetate form, has a broad range of applications such as drug release systems,[18–20] nucleation supports,[21] anti-counterfeit measures,[22] advanced shape-memory materials,[23] in composite and fog water collectors or tissue scaffolds.[10,24,25] The piezoelectric properties of cellulose acetate and its derivatives *i.e.* cellulose triacetate were reported for both crystalline and amorphous phases.[26,27] The piezoelectricity of cellulose shows many advantages in supporting the extracellular matrix of bone which is known for its piezoelectricity.[28] However, the piezoelectric properties of electrospun cellulose acetate (CA) fibers are yet to be reported. CA fibers have been researched as a replacement for bone tissue in their pure form as well as, with the addition of hydroxyapatite and its similarity to collagen has been hinted at before.[29–31] Notably, cellulose is mostly biologically inert but not biodegradable in humans, making it a permanent implant when inserted into a tissue.[13] As such, the material provides long-lasting structural support allowing for correct osseointegration much needed in bone replacement materials, however it may never be totally replaced by new native tissue.[16]

The biological behavior of cells is often regulated by the environment surrounding them. In the case of nanofiber-

---

[a] *Faculty of Metals Engineering and Industrial Computer Science, AGH University of Science and Technology, Al. Mickiewicza 30, 30-059 Kraków, Poland. E-mail: ustachew@agh.edu.pl*

[b] *Academic Centre for Materials and Nanotechnology, AGH University of Science and Technology, Poland*

[c] *Faculty of Physics and Applied Computer Science, AGH University of Science and Technology, Poland*

† Electronic supplementary information (ESI) available. See DOI: https://doi.org/10.1039/d3nr00014a

based scaffolds, it is their chemical composition, surface properties and morphology.[2] Especially surface potential of biomaterials has a significant effect on protein absorption and their binding, followed by more advanced biological effects found in both *in vitro* and *in vivo* studies. Generally, surface properties have been shown to alter protein adhesion, cell response and collagen formation.[32–34] Interestingly, only by changing the morphology of biomaterials may we cause cytotoxicity effects leading to cell damage.[2] Additionally, alignment of the fibers in scaffolds, yarns and weaves controls the directions of cell growth.[35,36] For electrospun scaffolds all above mentioned properties can be adjusted during manufacturing, avoiding additional postprocessing steps, which makes them a great candidate for tissue engineering.[37–39]

Piezoelectric materials modulate cellular behavior *via* surface charges generated in response to cellular interaction and vibration stimulus.[32] *In vivo* studies have shown increased cell activity for PVDF scaffolds implanted in rats.[40] However, the increased activity of osteoblast and bone marrow mesenchymal cells on piezoelectric materials was reported even without additional stimulation.[32] Additionally, changes in the electrical environment of fractured bones were reported.[41] Thus, restoring the original microenvironment *via* charges from transplanted material can be a prime cue for improving bone regeneration.[42] The polarized nanocomposite membranes composed of $BaTiO_3$ and poly(vinylidene fluoride tetrafluoroethylene) (P(VDF-TrFE) encouraged the osteogenic behavior *in vitro* and bone defect healing through sustainably maintained electric microenvironment *in vivo*.[42] Here, the stability of the materials' surface potential has been confirmed up to 12 weeks after implantation into bone defects.[42] The increased cell activity can also be achieved by the polarization of the scaffolds. It allows miming the original conditions for cells by providing the physiological electrical microenvironment.[42,43] Importantly, the stress exerted by cells during attachment to scaffolds and migration is enough to generate electrical signals.[44] The local properties directly affect cellular behavior as even the slightest changes in surface potential matter with the low piezoelectric coefficient materials.[32]

Electrospinning is an electrohydrodynamic process in which high voltage is used to produce nanofibers from a polymer solution.[45] High voltage is applied to elongate and extrude the polymer solution from a nozzle which is continuously supplied with a syringe pump. When the polymer solution is ejected, it forms a cone-jet due to the electrostatic forces. Then the solvent from the jet starts evaporating and fibers are deposited on the collector. Usually, the result of electrospinning is a non-woven mesh of polymer fibers.[45] The processing parameters, in electrospinning allow to obtain a wide array of shapes, sizes and mechanical properties of fibers from the same material.[45,46] Additionally, wettability can be controlled with processing parameters and post-treatment of electrospun fibers.[47,48] Electrospinning enhances the piezoelectric properties and surface potential of fibers, which can inhibit or hinder cell adhesion to fibers in tissue scaffolds.[33,46,49,50] Notably, surface properties, including potential of materials, play a critical role in protein adsorption as well as in early phases of cell attachment and initiates focal adhesion to the scaffolds.[51,52] In other medical applications surface potential and functionalization of electrospun fibers is crucial, *e.g.* in stimuli-responsive face masks.[53] The geometrical parameters of electrospun membranes and meshes *i.e.*, pore size, fiber to fiber distance or height of tissue scaffold, are tunable *via* electrospinning as well.[45,54] Those properties were successfully implemented to prepare injectable biomaterials.[55] This tunability of electrospun scaffolds is a great asset as the biochemistry of used surface and the environment affect cell morphology, adhesion and proliferation.[56] Thus, electrospinning can be used to prepare advanced tissue scaffolds from CA, taking advantage of its remarkable properties.[45]

CA is an ester form of cellulose, which is spinnable due to solubility in a few solvents. CA was electrospun and modified in various ways to obtain 3D scaffolds for bone tissue regeneration.[57] The electrospun core–shell structures based on CA and polycaprolactone (PCL) were manufactured to deliver active compounds such as curcumin, not only for biomedical applications, but for food packaging too.[58] Mechanical properties of pristine electrospun CA were reported, with tensile strength reaching about 0.2 MPa and the possibility of improvement with the KCl treatment.[25,59] Although the CA is used in many studies related to biomaterials including various modifications, especially in form of scaffold, the challenges related to understanding the fundamental interactions between cells and manufactured CA based materials remain. Therefore, this work focuses on developing a functional electrospun tissue scaffold from pure CA to create an electrical environment able to mimic natural conditions for cells. To verify the biocompatibility of CA fibers and their potential application in bioengineering, a series of experiments characterizing the behavior of cells was carried out using confocal laser scanning microscopy (CLSM). The electrospun CA scaffolds' properties were carefully investigated, especially in terms of surface properties as it is proven that surface potential affects cells development. The electrospun CA fibers are here first time explored in terms of not only surface potential but also piezoelectricity. Indeed, it is the first time reporting the piezoelectric properties of CA fibers and their surface potential effect on osteoblasts and further regeneration processes. Our findings demonstrate that electrospun CA allows osteoblast-like cells to form a vast 3D network of collagen fibers which is strictly limited to only typical 2D on a flat surface.

2. Results and discussion

2.1. Material characterization

Morphology investigation of electrospun fibers was performed using a scanning electron microscope (SEM), see Fig. 1a. CA fibers had an average fiber diameter of 540 ± 160 nm. A similar average diameter of fibers was previously reported.[60]

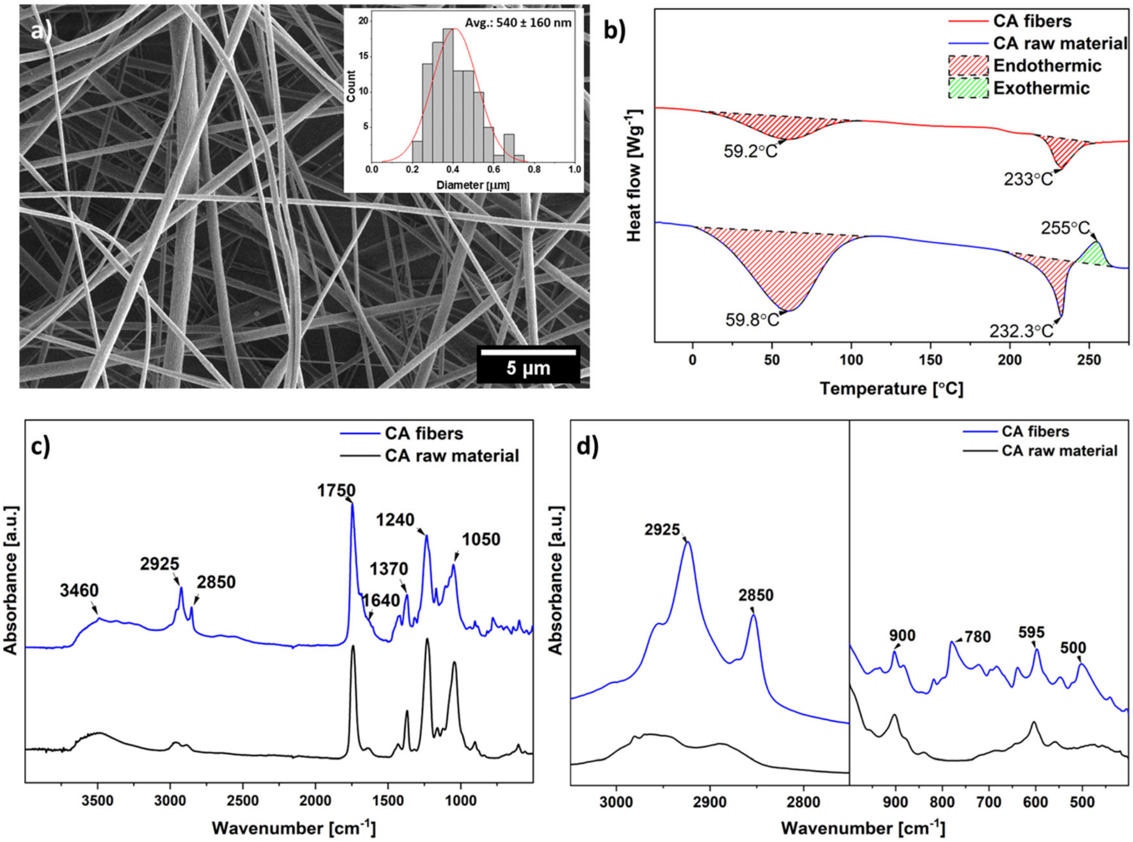

Fig. 1 Materials characterization, (a) SEM micrographs of electrospun CA fibers with their diameter distribution, (b) DSC thermal curves of CA samples for the first melting measurement, (c) FTIR-ATR spectra with (d) fingerprint regions of CA raw material and electrospun fibers.

Contact angle measurements (Fig. S1a†), showed highly hydrophobic behavior (136.3 ± 4.2°) for electrospun fibers which is driven by the porosity, chemical composition at the surface and roughness of electrospun networks.[61] The surface chemical composition investigation of CA fibers was performed using X-Ray photoelectron spectroscopy (XPS) at 45° angle, see Fig. S2.† The fibers had 23.4% C–C, 40.6% C–O and 36.1% O–C–O groups. The high content of O–C–O groups is likely caused by a high voltage applied during electrospinning, as a positive voltage polarity is known to attract negatively charged ions.[62]

Thermal analysis was carried out with differential scanning calorimetry (DSC), see Fig. 1b. Thermograms show the changes in melting regions between the CA samples. The maxima of peaks for melting were 233 and 232.3 °C for fibers and raw material, respectively. The crystallinity level was lowered *via* processing CA to 21.1% for electrospun fibers compared to 25.7% for raw material.

The chemistry of CA fibers was compared to raw material based on FTIR measurements presented in Fig. 1a. The peaks were also compared to literature values to check for potential shifts in the spectrum, see Table 1. The intensity of characteristic 1240 cm^{-1}$_{(\text{C–O})}$, 1370 cm^{-1}$_{(\text{–CH3})}$ and 1750 cm^{-1}$_{(\text{C=O})}$ peaks increase with the amount of cellulose triacetate (CTA) and represent important acetyl group vibrations.[63] The peaks

Table 1 The FTIR peak shift relative to literature reference with explanation of the corresponding bond from FTIR spectra

CA fibers Wavenumber (cm^{-1})	CA raw material	Literature value[63]	Corresponding bond
603	597	600	C–I stretching halo compound
––	780	780	C–H bending 1,2,3-trisubstituted
902	903	900	C–H bending 1,2,4-trisubstituted or 1,3-disubstituted
1044	1050	1050	C–O–C of the cellulose backbone
1230	1234	1240	C–O stretching of the acetyl group
1369	1371	1370	C–H bending vibration of CH_3 in the acetyl group
1741	1746	1750	C=O stretching of the acetyl group
2889–2963	2853–2923	2850–2950	C–H stretching of CH_2 or CH_3
3502	3490	3460	–OH stretching of unacetylated cellulose

corresponding to CTA are slightly shifted towards lower wavenumbers (>10cm^{-1}) indicating processing effects on CA.

Characteristic 1050 cm^{-1}$_{(C–O–C)}$ and 1750 cm^{-1}$_{(C=O)}$ peaks were selected for peak-to-peak ratio calculation. The results were 1.21 and 2.09 for CA fibers and CA raw material, respectively. The peak at 1050 cm^{-1}$_{(C–O–C)}$ which is not affected by acetylation shows that electrospinning changes the chemical structure of CA as the ratio is lower for fibers than for raw material, and the peak is broadened.[63] High peaks visible in the range of 2850–2950 cm^{-1} shown in Fig. 1b for CA fibers spectra correspond to the C–H stretch of CH_2 and CH_3 groups.

Further, we investigated the surface potential of CA fibers utilizing a Kelvin probe force microscope (KPFM). In Fig. 2a, we show the topographic image of electrospun fiber with a diameter of 671 ± 5 nm with a smooth surface. The atomic force microscopy (AFM) results confirmed the observations from SEM, regarding fibers diameter and morphology. The surface potential (Fig. 2b) measured with KPFM of CA fibers was, at an average 718 ± 4 mV indicating an effect of applied charges during electrospinning.[64] Surface properties over a larger area were verified with the streaming zeta potential measurements. In Fig. 2c, the zeta potential decrease with an increase of pH value from 3 to 9 is presented for CA electrospun fibers. A zeta potential of −12.2 ± 0.4 mV was recorded for pH in a range of 7–8 which overlaps with the pH of the cell medium solution of 7.5. Nair *et al.*, reported a matching zeta potential of −14.2 ± 1.1 mV for pH of 7.5 on electrospun CA fibers.[65] Similarly, other research indicated zeta potential of −12.5 ± 0.3 mV for nanofibers and −12.1 ± 0.3 mV for microfibers.[66] Glass, which was used as a control for cell studies, had a zeta potential of −60.1 ± 11.5 mV for pH of 7.5 and is in line with previous reports.[67] The isoelectric points, where zeta potential equals 0 mV, occurred at pH 4.14 for CA fibers. We did not observe the isoelectric point for glass, which is in pH below 3 that is out of range for our instrument. The negative value of zeta potential is possibly caused by a high content of negatively charged O–C–O groups observed in XPS. Thus, we conclude that electrospinning can affect the surface potential of processed CA fibers, as it was previously showed in electrospun poly(methyl methacrylate) (PMMA), polycaprolactone (PCL) and polyvinylidene fluoride (PVDF).[33,34,68]

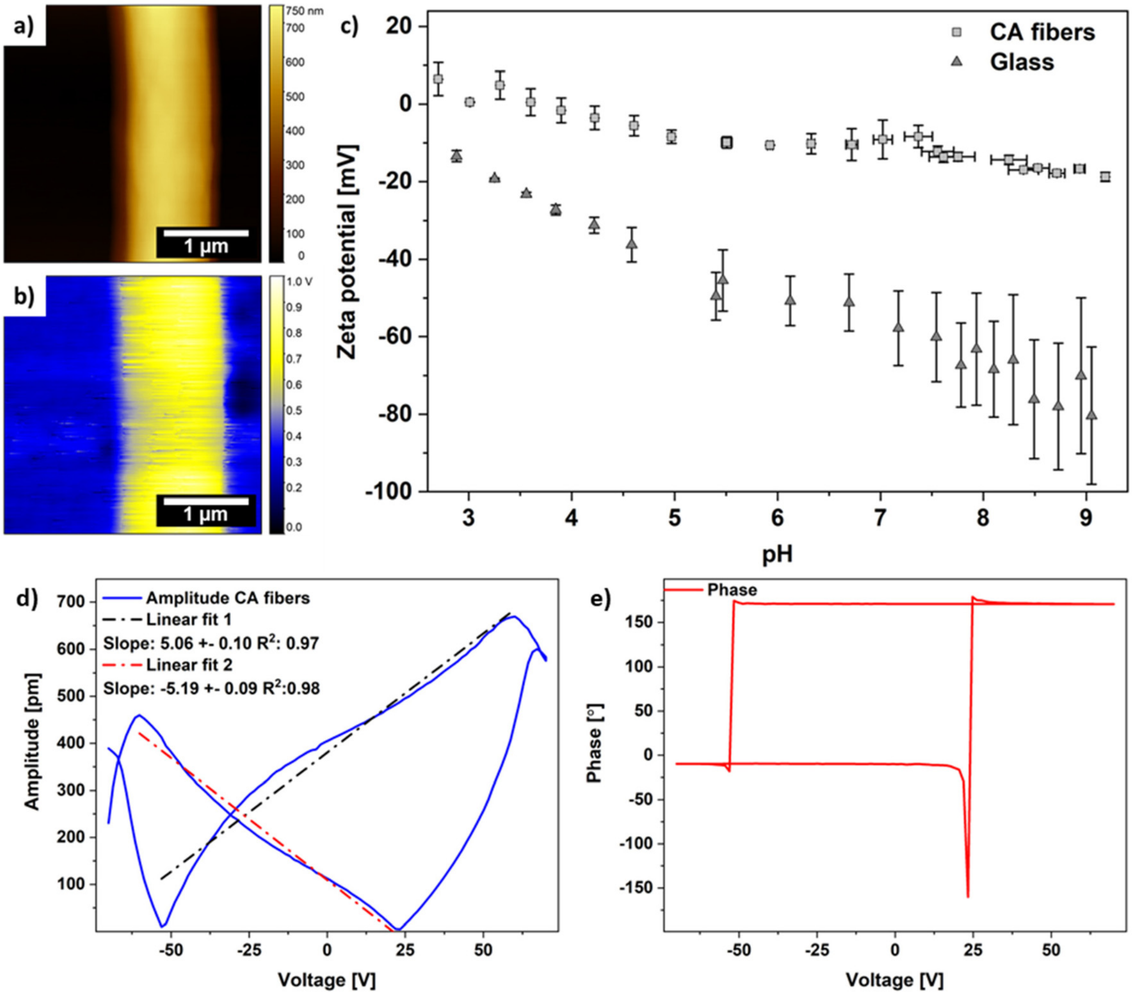

Fig. 2 Topography map (a) CA fibers with its respective (b) surface potential map from KPFM measurement, (c) zeta potential measurement plot. Plots represent (d) amplitude *versus* voltage with a line fit used for piezoresponse coefficient calculation and (e) phase switching *versus* voltage.

After surface potential measurements, the piezoelectric properties of the CA fibers were verified. To determine piezoelectric behavior, CA fibers were studied using high voltage switching spectroscopy piezoresponse force microscopy (HVSS-PFM). The HVSS-PFM measurements shown in Fig. 2d and e, were recorded by charging the material in 50 ms steps from −70 to 0 V, then from 0 to 70 V and back from 70 to −70 V with the tip kept at a fixed position on the surface of the CA fiber. The used DC voltage range of 140 V was found to be set beyond the coercive field of the material. Furthermore, 50 ms voltage pulses led to phase switching, meaning high switching sensitivity of the CA fibers. In Fig. 2d, the amplitude–voltage butterfly loop is shown. The highest amplitude of 669.2 pm at V_{dc} of 60 V was observed. The polarization reversal occurs at the coercive field, which changes the sign of the surface charges, causing the phase switch of 180°, see Fig. 2e. Both phase and voltage loops have shown good repeatability and are asymmetric due to the non-uniform distribution of charge defects.[69] As previously indicated,[70] we observed the piezoelectric behavior only in the shear d_{31} direction, which in our case for CA fibers reached 6.68 ± 1.70 pmV^{-1}. No PFM signal apart from noise was observed for the d_{33} coefficient, see Fig. S3.† Importantly, the piezoelectric properties depend on size,[71] and here the measured CA fiber had a diameter of 393 ± 8 nm. The d_{33} coefficient for PVDF fiber (300 nm), a highly piezoelectric polymer, was 17.6 pmV^{-1}.[71] The obtained piezoelectric response proved the piezoelectric properties of electrospun CA fibers.

2.2. Cell culture studies

The mean density of cells was estimated at 1, 2 and 4 h after seeding to evaluate the adhesion capacity of cells to CA scaffolds (Fig. 3a). Exemplary micrographs from confocal microscopy used for adhesion calculations are shown in Fig. S4.† The cells seeded on CA fibers showed an increased density in time. After 1 h of incubation, on average, 15.7 ± 11.2 cells per 1 mm^2 were attached to the scaffold, which then increased to 40.3 ± 3.1 and 88.5 ± 30 cells for 2 h and 4 h, respectively. Results on glass control for 1 h and 2 h are similar to CA fibers however, at 4 h the cell density is lower (53.2 ± 30.3 cells per 1 mm^2). The sharp increase of cell adhesion to the CA scaffold is caused by cells forming more

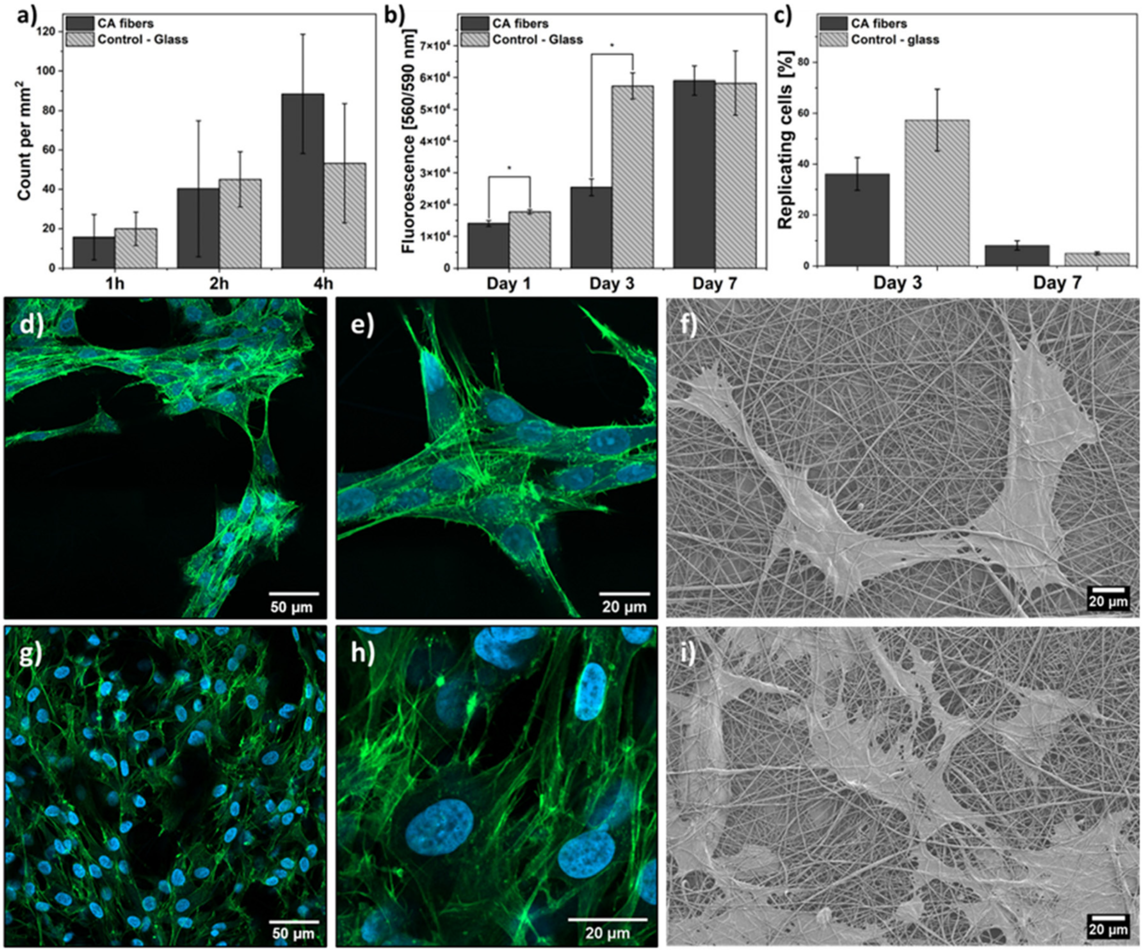

Fig. 3 Cell culture results from (a) adhesion test, (b) proliferation and (c) replication test. Actin fibers imaging from confocal microscopy with corresponding SEM images of cells growing on CA fibers at (d–f) day 3 and (g–i) day 7 of cell culture. The nuclei were stained with DAPI (blue) and the actin filaments with Alexa Fluor™ 488 Phalloidin (green). *Differences were considered statistically significant when $p < 0.05$.

focal adhesion sites, which causes their stronger adherence to the surface.

Cell proliferation on CA fibers was tested over 7 days of incubation, see Fig. 3b, where the fluorescence signal is proportional to the number of viable cells. The cell proliferation profiles differ for CA scaffolds and the control glass. For CA fibers, proliferation continuously increases over 7 days, showing stable growth in opposition to the control sample, which reached a plateau after 3 days in cell culture. This difference can be explained by cells still being in the logarithmic phase of multiplication on the glass, while CA scaffolds require more time for cells to proliferate.[72]

The replication tests complemented the proliferation results by showing how many cells are in the replication stadium of growth and their location in the cell colony, see Fig. S5.† Emitted green, fluorescent signal from part of cells comes from labeling precursor EdU, which was incorporated to new synthesized DNA strain during the replication process. Fig. 3c presents the replication activity of cells growing on CA fibers and glass as control after 3 and 7 days. On fibers after 3 days, around 36% of growing cells show a signal of an ongoing replication process. After 7 days, many more cells were visible within the imaging area, but only 8% were replicating among them. On the glass control, after 3 days, 57% of cells showed an ongoing replication process. In contrast, after day 7, when the cells number is much higher and all available space is occupied, only 5% of cells emitted a green signal. As confocal imaging shows one plane, we see all cells on a flat 2D surface of the glass, while cells in 3D scaffolds grow at the surface and inside the porous structure, between the fibers (see an animation in the ESI Video 1†). Therefore, we see a lower cell number compared to the proliferation test (Fig. S5†). In cell studies, actin imaging was also carried out to investigate actin cytoskeleton structure related to cell shape, elongation, distribution, and binding to CA samples. Fig. 3 shows microphotographs from CLSM imaging of actin fibers and respective SEM images of cells cultured on CA fibers. Cells growing on fibers stretched along their length and formed multiple connections and filopodia in all directions, as observed in all stages of development. In addition, the material was evenly populated with cells, and there were no signs of abnormal shapes. Such behavior indicates supreme compatibility of the material with cells and a positive influence of 3D structure on the cell–material interaction. Furthermore, lamellipodium spreading in all directions of 3D space on CA fibers is visible, leading to many binding sites. This finding contrasts with cell growth on the glass, where the spreading is comparable. However, it only takes place in 2D space, see Fig. S6.†

In bone tissue engineering, collagen production by cells is the key to speeding up the regeneration processes.[73] We performed a collagen detection test after 7 days of cell culture to investigate the advantages of CA as a supportive scaffold (see Fig. 4). All imaging parameters were constant for each magnification. On CA fibers (Fig. 4a and b), cells created a highly branched collagen fibers network forming a 3D structure (see an animation in the ESI Video 1†). The such a 3D structure closely resembles the extracellular matrix (ECM) of a living organism.[74] Moreover, we observed high collagen concentration, showing an increased affinity of cells to the fibrous CA scaffold and their great potential in bone tissue regeneration. On glass control, we observed a 2D collagen matrix around cells growing on the surface of the substrate (Fig. 4c and d), which confirms good cell development on glass. However, the signal from collagen on glass is weaker compared to CA fibers indicating lower protein concentration.

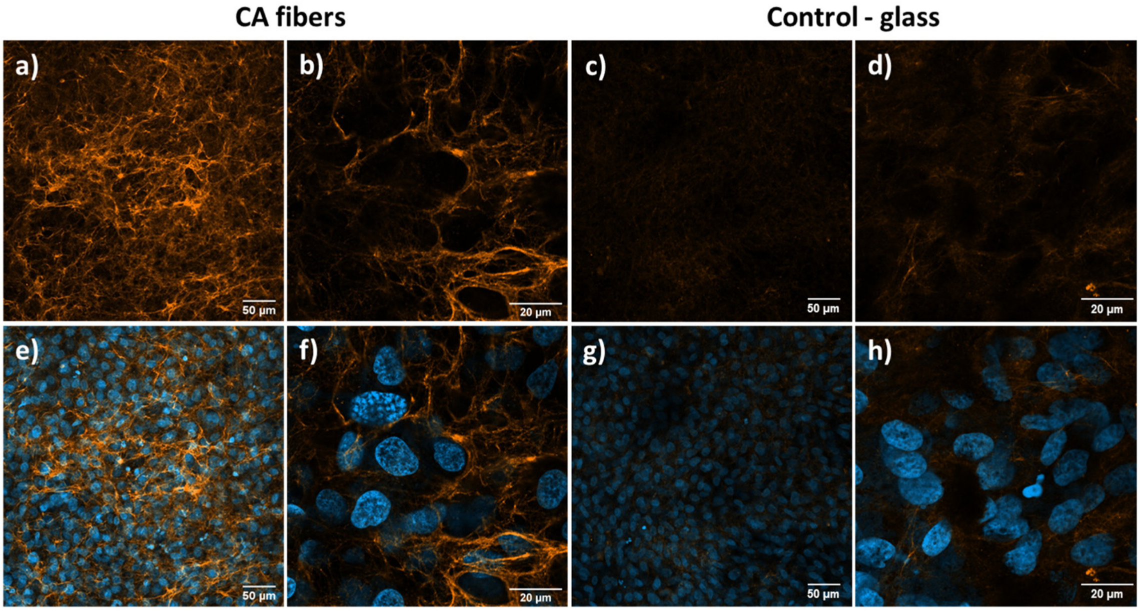

Fig. 4 Collagen staining results after 7 days of cell culture, (a, c, e and g) low magnification, (b, d, f and h) high magnification as observed with CLSM. The nuclei were stained with DAPI (blue) and collagen with Alexa Fluor™ Plus 555 (orange).

The imaging results from collagen staining complement what we observed *via* confocal microscopy studies of actin fibers and replication tests. We notice the stretching of well-developed cells from fiber to fiber in CA scaffolds, forming a vast 3D network rich in collagen. Such growth is caused by the synergistic effect of a high surface area to volume ratio of electrospun fibers and the benefits of elevated surface and zeta potentials, as well as the piezoelectric properties of the material.[34]

When comparing CA fibers to glass control, we observed significant differences in cell behavior with all carried-out tests and microscopy investigations. Distribution patterns of MG-63 cells formed depending on culture substrate. Scaffolds of electrospun CA fibers led to intermingled, randomly distributed patches of cells growing on the material with spread out cytoskeletons. Such behavior is caused by a highly developed and rough layout of fibers providing space for cell proliferation coupled with many attachment points for filopodia giving it an edge over the smooth glass.[34] Moreover, KPFM and zeta potential measurements have shown that CA fibers have high surface potential favored by cells which also contributes to improved growth.[34,52,75] Previous reports have shown that modification of surface potential for PVDF and PCL fibers significantly affects anchoring, proliferation, mineralization and collagen formation for osteoblast-like cells.[33,76] Additionally, piezoelectric properties of the fibers provide a similar environment to native tissue. These differences confirm that cell scaffold architecture and surface properties are crucial and complementary to each other for enhanced attachment, proliferation, and growth of cells leading to a critically stimulated bone tissue regeneration process.

The piezoelectric coefficient of the bone itself is low, reaching 0.1 to 0.7 pmV^{-1}.[77,78] Therefore, the d_{31} = 6.68 ± 1.70 pmV^{-1} for CA fibers provides stronger stimuli than the natural environment for cell, contributing to excellent collagen formation. Similarly to previous reports, cell activities on CA fibers are enhanced by a high surface potential of 718 ± 4 mV and zeta potential of −12.2 ± 0.4 mV, which are known to improve cellular response in tissue engineering.[32,42,79]

3. Conclusion

In this study, we showed that electrospun CA fibers provide a superb scaffold for bone cells. The cell studies showed the enormous effect of surface properties and geometry of CA on cell adhesion, proliferation, and growth. We also presented for the first-time piezoelectric properties of electrospun CA scaffolds using the HVSS-PFM technique. Piezoelectric coefficient of d_{31} = 6.68 ± 1.70 pmV^{-1} along with high surface (718 mV) and zeta (−12.2 mV) potentials allowed us to mimic natural electrical environment favoring bone cells attachment and growth. Furthermore, with advanced CLSM, we could indicate high cell replication on CA scaffolds after 7 days of culture compared to the typical 2D control sample. Cells spreading, a pattern of actin fibers and very early ECM formation, visualized by a vast 3D network of collagen fibers, are proof of the excellent environment for bone cells. In tissue engineering studies, the entire microenvironment created by the scaffold provided permanent mechanical support. Notably, the geometry and surface properties creating the electrostatic interactions between material and cells must be considered to understand material-driven tissue development better. Therefore, our work investigated the piezoelectric electrospun CA fibers with the desired surface potential to show a promising solution for long-lasting structural support needed as a bone replacement biomaterial. Our results are focused primarily on the early stages of osteogenesis, cell integration, spreading and collagen expression in response to CA fibers. Further studies are necessary to bridge the gap between early-stage bone formation and osteoprogenitor cell differentiation.

4. Experimental section

4.1. Sample preparation: electrospinning

Cellulose acetate (CA, product number 419 028-500G, average $M_n \approx 50\,000$ by GPC, Sigma Aldrich, USA) with an extent of labeling of 39.7 wt% acetyl (as stated by supplier) was dissolved in dimethylacetamide (DMAC, for HPLC, POCH, Poland) and acetone (pure, POCH, Poland) with 1 : 1 (v/v) ratio to obtain 19% solution on a magnetic stirrer with a heating plate (IKA RCT basic, Staufen, Germany) using 150 rpm at T = 25 °C and RH = 30% for 5 h.

Electrospinning was carried out using an apparatus with a climate upgrade system (IME Technologies, The Netherlands) at constant T = 25 °C and RH = 70%. Electrospinning parameters were as follows: 13 kV potential difference, 20 cm nozzle to collector distance, 0.1 mlh^{-1} solution flow rate, 0.5 mm inner and 0.8 mm outer diameters of the needle (KD Fine, 0.8 × 40 mm, 21G). CA fibers were prepared at 15 × 15 mm Si wafers sputter coated (Q150RS, Quorum Technologies, Laughton, UK) with a 20 nm layer of Au to ensure sample conductivity during KPFM and PFM measurements. For the cell culture study, fibers were collected on round cover glasses (Menzel Gläser, Germany) with a diameter of 13 mm. For the zeta potential study fibrous membrane was electrospun for 4 h.

4.2. Characterization of CA fibers

Advancing contact angles on electrospun fibers were measured by pipetting droplets of 3 μL volume on the surfaces using deionized (DI) water (Spring 5UV purification system - Hydrolab, Poland). Experiments were carried out at a T = 23 °C and RH of 45%. The images of droplets were taken using a Canon EOS 700D camera with EF-S 60 mm f/2.8 Macro USM zoom lens immediately after the liquid deposition. The advancing contact angle was measured using ImageJ software (v.1.51 g, NIH, USA). The average contact angle ± standard deviation was calculated from 10 separate measurements using OriginPro.

Scanning electron microscopy (SEM, Merlin Gemini II, Zeiss, Germany) was carried out to investigate the morphology of cellulose fibers. All samples were sputter-coated with a 5 nm Au layer before imaging using a rotary-pump sputter coater. An accelerating voltage of 3 kV with a current of 150 pA at a working distance of 6–10 mm were used for all investigated samples. Fiber diameters were measured on 100 fibers using ImageJ. The average fiber diameter ± standard deviation was calculated using OriginPro (v9.7.0.188, OriginLab Corporation, USA).

X-ray photoelectron spectroscopy (XPS, VersaProbe II XPS System, PHI, USA) measurements were carried out at a 45° angle using aluminum Kα (1486.6 eV) monochromatic radiation focused to a 100 μm spot. Chamber pressure was kept below 4×10^{-9} mbar. To obtain high-energy resolution spectra of investigated materials, the pass energy in the analyzer was set to 23.5 eV and 0.1 eV step. A dual-beam charge compensation system with 7 eV Ar + ions and 1 eV electrons was used to ensure the constant surface potential of analyzed samples. Obtained spectra were deconvoluted with MultiPak software (PHI, USA) using the Shirley method for spectrum background subtraction.

The molecular structure of CA was investigated with Fourier transform infrared spectroscopy (FTIR, Nicolet iS5, Thermo Fisher Scientific, USA). Obtained fibers prepared 24 h prior to the tests were compared to raw material in the form of powder. For each sample, 32 scans with a resolution of 4 cm^{-1} in the 400–4000 cm^{-1} range were performed.

Thermal analysis was carried out with differential scanning calorimetry (DSC 3, Mettler Toledo, Switzerland) at a heating rate of 10 Kmin^{-1} from −25 to 275 °C. For statistics, three separate samples of fibers and raw material were examined. Presented values are averaged from 3 independent tests. For crystallinity calculation, the value for the enthalpy of fusion of a perfect crystal of cellulose acetate of 58.8 Jg^{-1} was used as previously reported.[80]

Kelvin probe force microscopy (KPFM) mode of CoreAFM (Nanosurf, Switzerland) was used to measure topography and surface potential. For KPFM, conductive HQ:NSC18/PT (MikroMasch, Bulgaria) tips with a force constant of 2.8 Nm^{-1} and a resonance frequency of 75 kHz were used. Surface topography was measured on the area of 3 × 3 μm. For KPFM, the calculation of average surface potential was carried out using OriginPro. All calculations were carried out from 3 different regions on the KPFM scan. The surface potential measurements were carried out right after 24 h drying cycle of fibers, as surface potential decay is a well-known phenomenon for CA films.[81] Moreover, the measurements were carried out on a twin set of samples simultaneously to the cell culture studies beginning. This approach gives a surface potential value that closely matches the material that interacted with cells.

High voltage switching spectroscopy piezoresponse force microscopy (HVSS-PFM) was carried out using a CoreAFM microscope. A complete description of the method has been previously reported.[82] This method is employed to negate parasitic electrostatic and electrochemical effects by working in pulses. In this technique, local piezoelectric response of the material is detected using conducting AFM cantilever. The phase of the deflection provides information on the polarization direction. A phase of the deflection carries information on the coercive bias, polarization value and polarization direction, which provide complete information of the polarization behavior of the material. The amplitude of the deflection is used to reproduce the deformation of the measured material and can be reconstructed to provide a piezoelectric coefficient of the material. For measurements, conductive ElectriCont-G (BudgetSensors, Bulgaria) tips with a force constant of 0.2 Nm^{-1} and a resonance frequency of 13 kHz were used. A complete method description has been previously reported.[82] In this study voltage range of 140 V within 200 steps and a pulse time of 50 ms were used. Piezoresponse in d_{31} direction was calculated from 3 separate measurements, 10 separate fibers were measured to ensure that no piezoelectricity in d_{33} direction is present in the samples. Slopes of the amplitude loops were used to obtain the piezoelectric coefficient of the material and are given as an average of 6 slopes constructed from 3 separate tests. For the calculation of the piezoelectric coefficient from butterfly curves, we followed the previous reports.[71]

The streaming zeta potential was measured using an electrokinetic analyzer (SurPASS 3, Anton Paar, Austria). The measurement was performed with pH steps of 0.3 in acidic (3.0–5.6) and basic (5.6–9.0) pH ranges. The pH of the 0.01 M initial solution of KCl was changed by the progressive addition of 0.1 M HCl or 0.1 M NaOH. After titrations, samples were rinsed 3 times with KCl solution possessing a new pH value, and then the zeta potential was measured 4 times. For streaming zeta potential, a specialized holder for porous materials was used to negate the possibility of damage on CA fibers by electrolyte flow in the capillary channel. The fibrous network was put into the cylindrical cell with a permeability index of 220 μm, where the solution was flowing freely between the fibers.

4.3. Cell culture studies and imaging

The *in vitro* studies were performed on CA fibers using human osteoblast-like cell line MG-63 (Sigma-Aldrich, USA). The cover glass was used as a control sample for all cell culture tests. Samples on cover glasses were placed in 24-well plates and sterilized for 30 min in UV light. Cells were seeded in the scaffolds at a concentration of 2×10^4 cells per 1 ml in culture media containing Dulbecco's Modified Eagle Medium supplemented with 10% fetal bovine serum (FBS), 2% antibiotics (penicillin/streptomycin), 1% amino acids, and 1% L-glutamine (all reagents from Sigma-Aldrich, USA). Samples with cells were incubated in 37 °C, RH = 90%, and 5% CO_2 atmosphere for up to 7 days. The medium was replaced every 2 days.

Cell proliferation was verified after 1, 3 and 7 days of incubation, samples with attached cells were removed from the supportive cover glass and transferred to a new plate. This was done to ensure that we investigate only cells that adhered and proliferated on the surface of tested materials. Subsequently, 400 μl of fresh media with 80 μl of CellTiter-Blue® reagent was added and incubated for 4 h at 37 °C. From each well, 100 μm of reagent was transferred to a 96-well plate in triplicates, and fluorescence was read at 560/590 nm using the microplate reader GloMax® Discover System (Promega, USA). For each sample type, 5 replicates were tested.

To study cells morphology, samples were fixed after 1, 3 and 7 days of incubation with 2.5% glutaraldehyde (Sigma-Aldrich, USA) for 1 h in $T = 23$ °C. Afterward, they were washed 3 times with phosphate-buffered saline (PBS, Biomed Lublin, Poland) and dehydrated in a series of ethanol (Avantor, Poland) solutions, with increasing alcohol content (30%, 50%, 70%, 90%, 100%). Incubation in each ethanol solution was done for 5 min. The final dehydration step was double incubation in 100% ethanol for 10 min, followed by incubation in Hexamethyldisilazane (HMDS, Sigma Aldrich, USA) under a fume hood until complete evaporation of the solvent. The samples were mounted at Al holders by carbon tape and gold-sputtered with an 8 nm layer. The samples were imaged by SEM (Merlin, Zeiss) using the same setting as for the materials.

In the adhesion test, after 1, 2 and 4 h, samples were washed with PBS to rinse off non-attached cells and then fixed in 4% paraformaldehyde solution for 15 min at 23 °C. Cell nuclei were stained with 4', 6-Diamidino-2-phenylindole (DAPI, Sigma Aldrich, USA) for 5 min (1 : 1000, in all experiments). For all steps, separate samples were used. The same cell culture solution was seeded onto all the substrates. Washing has been carried out exactly after the respective time of culture was reached.

For replication tests, before fixation, the cell cultures were treated with 10 μM of 5-ethynyl-2′-deoxyuridine (EdU) for 1 h. Then, they were washed with PBS, fixed with 4% paraformaldehyde, followed by permeabilization, and blocking in 0.1% Triton X-100 (Sigma) and 3% bovine serum albumin (Sigma Aldrich, USA) at 25 °C, respectively. The Click-iT™ EdU AF488 imaging kit (Invitrogen/Molecular Probes) was used to detect incorporated a thymidine analog EdU (5-ethynyl-2′-deoxyuridine). The cells were then counterstained with DAPI for 15 min.

Actin imaging was done on samples after 3 and 7 days. Cells were fixed in 4% paraformaldehyde solution for 15 min in 23 °C and washed two times with PBS. Then cells were permeabilized with 0.1% Triton X-100 in PBS for 10 min at 23 °C. To visualize actin filaments, cells were incubated for 1 h at $T = 23$ °C with Alexa Fluor™ 633 Phalloidin (Thermo Fisher Scientific, USA) and then washed three times in PBS. Nuclear DNA was stained with DAPI for 5 min. After staining, samples were washed three times (15 min each) with PBS.

Collagen imaging was carried out after 7 days cells were incubated for 1 h with monoclonal Anti-Collagen, Type I antibody (C2456, Merck, USA), followed by Goat anti-Mouse Secondary Antibody, Alexa Fluor Plus 555 (A32727, Thermo Fisher Scientific, USA) for 1 h. After incubations, the cells were rinsed with PBS (37 °C) and fixed with 4% formaldehyde in PBS for 15 min. Nuclei were counterstained with DAPI for 15 min.

4.4. Confocal laser scanning microscopy (CLSM)

Zeiss LSM 900 confocal microscope (Carl Zeiss Microscopy GmbH, Germany) was used to image fixed samples. Images were acquired using ZEN 3.1 software (Carl Zeiss Microscopy GmbH) and processed using ImageJ 1.53v (NIH, Bethesda, Maryland, USA). For excitation: 405 nm, 488 nm and 561 nm laser lines were used, emission detection bands were set to 410–570 nm for DAPI, 500–600 nm for Alexa Fluor™ 488 coupled with Phalloidin or labeled incorporated EdU, 540–700 nm for Alexa Fluor™ 555 respectively. For the cells' adhesion analysis, we used Plan-Apochromat 10×/0.45 M27 objective; pixel size 0.22 μm, the average number of cells per 1 mm^2 were quantified from at least ten random fields (1 × 1 mm) for each sample and for cell replication imaging: Plan-Apochromat 20×/0.8 M27 objective, pixel size 0.124 μm, the average density of replicated cells (shown in green) and all cells (shown in blue) per 1 mm^2 were quantified from at least ten random fields (1 × 1 mm) for each sample. Deviation in a ratio of replicated to all cells is calculated as an exact differential.

4.5. Statistics

Statistical analysis of cell proliferation, adhesion, and replication was done using one-way ANOVA followed by Tukey's *post hoc* test in OriginPro. Differences were considered statistically significant when $p < 0.05$.

Conflicts of interest

The authors declare that they have no known competing financial interests or personal relationships that could have appeared to influence the work reported in this paper.

Acknowledgements

This study was conducted with funding from the OPUS 17 project grant provided by the National Science Centre in Poland. No 2019/33/B/ST5/01311 and NAWA exchange program between Poland and China No PPN/BCN/2019/1/00067/U/00001. The confocal microscopy studies were performed by Krzysztof Berniak as a part of the "Nanofiber-based sponges for atopic skin treatment" project carried out within the First TEAM program of the Foundation for Polish Science co-financed by the European Union under the European Regional Development Fund, project No POIR.04.04.00-00-4571/17-00.

References

1 J. Courtenay, R. Sharma and J. Scott, *Molecules*, 2018, **23**, 654.
2 H. Xiang and Y. Chen, *View*, 2020, **1**, 20200016.
3 V. Hasırcı, K. Lewandrowski, J. D. Gresser, D. L. Wise and D. J. Trantolo, *J. Biotechnol.*, 2001, **86**, 135.

4 Z. J. Krysiak, J. Knapczyk-Korczak, G. Maniak and U. Stachewicz, *Colloids Surf., B*, 2021, **199**, 111554.
5 M. Sanaty and A. Temel, *Ophthalmologica*, 1998, **212**, 328.
6 V. Kudryavtseva, S. Boi, J. Read, D. Gould, P. K. Szewczyk, U. Stachewicz, M. v. Kiryukhin, L. Pastorino and G. B. Sukhorukov, *Mater. Des.*, 2021, **202**, 109527.
7 S. Sell, C. Barnes, M. Smith, M. McClure, P. Madurantakam, J. Grant, M. McManus and G. Bowlin, *Polym. Int.*, 2007, **56**, 1349.
8 M. S. Enayati, T. Behzad, P.Ł Sajkiewicz, R. Bagheri, L. Ghasemi-Mobarakeh and F. Pierini, *Cellulose*, 2018, **25**, 65.
9 D. Klemm, B. Heublein, H.-P. P. Fink and A. Bohn, *Angew. Chem., Int. Ed.*, 2005, **44**, 3358.
10 R. Konwarh, N. Karak and M. Misra, *Biotechnol. Adv.*, 2013, **31**, 421.
11 S. Fischer, K. Thümmler, B. Volkert, K. Hettrich, I. Schmidt and K. Fischer, *Macromol. Symp.*, 2008, **262**, 89.
12 I. Singh, A. Sharma and B.-D. Park, in *Nanoarchitectonics for Smart Delivery and Drug Targeting*, Elsevier, 2016, pp. 95–117.
13 R. J. Hickey and A. E. Pelling, *Front. Bioeng. Biotechnol.*, 2019, **7**, 45.
14 B. v. Mohite and S. v. Patil, *Biotechnol. Appl. Biochem.*, 2014, **61**, 101.
15 R. M. A. Domingues, M. E. Gomes and R. L. Reis, *Biomacromolecules*, 2014, **15**, 2327.
16 O. S. Manoukian, N. Sardashti, T. Stedman, K. Gailiunas, A. Ojha, A. Penalosa, C. Mancuso, M. Hobert and S. G. Kumbar, *Encycl. Biomater. Biomed. Eng.*, 2019, **3**, 462.
17 S. Gea, C. T. Reynolds, N. Roohpour, B. Wirjosentono, N. Soykeabkaew, E. Bilotti and T. Peijs, *Bioresour. Technol.*, 2011, **102**, 9105.
18 J. E. Sanders, Y. Han, T. S. Rushing and D. J. Gardner, *Nanomaterials*, 2019, **9**, 805.
19 M. M. Castillo-Ortega, A. Nájera-Luna, D. E. Rodríguez-Félix, J. C. Encinas, F. Rodríguez-Félix, J. Romero and P. J. Herrera-Franco, *Mater. Sci. Eng., C*, 2011, **31**, 1772.
20 Y. Yang, W. Li, D.-G. Yu, G. Wang, G. R. Williams and Z. Zhang, *Carbohydr. Polym.*, 2019, **203**, 228.
21 F. A. Müller, L. Müller, I. Hofmann, P. Greil, M. M. Wenzel and R. Staudenmaier, *Biomaterials*, 2006, **27**, 3955.
22 E. Hendrick, M. Frey, E. Herz and U. Wiesner, *J. Eng. Fibers Fabr.*, 2010, **5**, 21.
23 D. Aoki, Y. Teramoto and Y. Nishio, *Biomacromolecules*, 2007, **8**, 3749.
24 N. Chousidis, O. Charalambous, M. Zymaride, C. N. Christou, A. Christophi, I. Savva, L. Kyriakou, I. Ioannou and T. Krasia-Christoforou, *Fibers Polym.*, 2021, **22**, 676.
25 J. Knapczyk-Korczak, J. Zhu, D. P. Ura, P. K. Szewczyk, A. Gruszczyński, L. Benker, S. Agarwal and U. Stachewicz, *ACS Sustainable Chem. Eng.*, 2021, **9**, 180.
26 E. Fukada, M. Date and T. Emura, *J. Soc. Mater. Sci., Jpn.*, 1968, **17**, 335.
27 E. Fukada, *Q. Rev. Biophys.*, 1983, **16**, 59.
28 M. H. Shamos, L. S. Lavine and M. I. Shamos, *Nature*, 1963, **197**, 81.
29 Q. Shi, Y. Li, J. Sun, H. Zhang, L. Chen, B. Chen, H. Yang and Z. Wang, *Biomaterials*, 2012, **33**, 6644.
30 K. Li, J. Wang, X. Liu, X. Xiong and H. Liu, *Carbohydr. Polym.*, 2012, **90**, 1573.
31 K. Rodríguez, J. Sundberg, P. Gatenholm and S. Renneckar, *Carbohydr. Polym.*, 2014, **100**, 143.
32 B. Tandon, J. J. Blaker and S. H. Cartmell, *Acta Biomater.*, 2018, **73**, 1.
33 P. K. Szewczyk, S. Metwally, J. E. Karbowniczek, M. M. Marzec, E. Stodolak-Zych, A. Gruszczyński, A. Bernasik and U. Stachewicz, *ACS Biomater. Sci. Eng.*, 2019, **5**, 582.
34 S. Metwally, S. Ferraris, S. Spriano, Z. J. Krysiak, Ł. Kaniuk, M. M. Marzec, S. K. Kim, P. K. Szewczyk, A. Gruszczyński, M. Wytrwal-Sarna, J. E. Karbowniczek, A. Bernasik, S. Kar-Narayan and U. Stachewicz, *Mater. Des.*, 2020, **194**, 108915.
35 G. Jin, R. He, B. Sha, W. Li, H. Qing, R. Teng and F. Xu, *Mater. Sci. Eng., C*, 2018, **92**, 995.
36 X. Chen, A. Ergun, H. Gevgilili, S. Ozkan, D. M. Kalyon and H. Wang, *Biomaterials*, 2013, **34**, 8203.
37 P. Pedraz, S. Casado, V. Rodriguez, M. C. Giordano, F. B. de Mongeot, A. Ayuso-Sacido and E. Gnecco, *Nanotechnology*, 2016, **27**, 125301.
38 A. M. Alshehri, S. Hadjiantoniou, R. J. Hickey, Z. Al-Rekabi, J. L. Harden, A. E. Pelling and V. R. Bhardwaj, *Biomed. Mater.*, 2016, **11**, 015014.
39 V. v. Kiroshka, T. A. Yurchuk, N. v. Repin, V. A. Petrova, I. v. Gofman, Y. A. Skorik, E. v. Kiroshka and T. P. Bondarenko, *Bull. Exp. Biol. Med.*, 2014, **158**, 153.
40 A. Wang, Z. Liu, M. Hu, C. Wang, X. Zhang, B. Shi, Y. Fan, Y. Cui, Z. Li and K. Ren, *Nano Energy*, 2018, **43**, 63.
41 T. Zigman, S. Davila, I. Dobric, T. Antoljak, G. Augustin, D. Rajacic, T. Kovac and T. Ehrenfreund, *Injury*, 2013, **44**, S16.
42 X. Zhang, C. Zhang, Y. Lin, P. Hu, Y. Shen, K. Wang, S. Meng, Y. Chai, X. Dai, X. Liu, Y. Liu, X. Mo, C. Cao, S. Li, X. Deng and L. Chen, *ACS Nano*, 2016, **10**, 7279.
43 S. S. Hur, Y. Zhao, Y. S. Li, E. Botvinick and S. Chien, *Cell. Mol. Bioeng.*, 2009, **2**, 425.
44 A. Zaszczynska, P. Sajkiewicz and A. Gradys, *Polymers*, 2020, **12**, 161.
45 P. K. Szewczyk and U. Stachewicz, *Adv. Colloid Interface Sci.*, 2020, **286**, 102315.
46 D. P. Ura, J. Rosell-Llompart, A. Zaszczyńska, G. Vasilyev, A. Gradys, P. K. Szewczyk, J. Knapczyk-Korczak, R. Avrahami, A. O. Šišková, A. Arinstein, P. Sajkiewicz, E. Zussman and U. Stachewicz, *Materials*, 2020, **13**, 4169.
47 H. Wu, R. Zhang, Y. Sun, D. Lin, Z. Sun, W. Pan and P. Downs, *Soft Matter*, 2008, **4**, 2429.
48 R. S. Kurusu and N. R. Demarquette, *Int. Mater. Rev.*, 2019, **64**, 249.
49 P. K. Szewczyk, A. Gradys, S. K. Kim, L. Persano, M. Marzec, A. Kryshtal, T. Busolo, A. Toncelli, D. Pisignano,

A. Bernasik, S. Kar-Narayan, P. Sajkiewicz and U. Stachewicz, *ACS Appl. Mater. Interfaces*, 2020, **12**, 13575.

50 W.-L. Kao, H.-Y. Chang, K.-Y. Lin, Y.-W. Lee and J.-J. Shyue, *J. Phys. Chem. C*, 2017, **121**, 533.

51 A. Gessner, A. Lieske, B. R. Paulke and R. H. Müller, *J. Biomed. Mater. Res., Part A*, 2003, **65**, 319.

52 S. Metwally and U. Stachewicz, *Mater. Sci. Eng., C*, 2019, **104**, 109883.

53 A. Zakrzewska, M. A. Haghighat Bayan, P. Nakielski, F. Petronella, L. de Sio and F. Pierini, *ACS Appl. Mater. Interfaces*, 2022, **14**(41), 46123–46144.

54 P. R. Buenzli, M. Lanaro, C. S. Wong, M. P. McLaughlin, M. C. Allenby, M. A. Woodruff and M. J. Simpson, *Acta Biomater.*, 2020, **114**, 285.

55 P. Nakielski, C. Rinoldi, M. Pruchniewski, S. Pawłowska, M. Gazińska, B. Strojny, D. Rybak, K. Jezierska-Woźniak, O. Urbanek, P. Denis, E. Sinderewicz, W. Czelejewska, J. Staszkiewicz-Chodor, M. Grodzik, Y. Ziai, M. Barczewska, W. Maksymowicz and F. Pierini, *Small*, 2022, **18**, 2104971.

56 R. Kurpanik and E. Stodolak-Zych, *Eng. Biomater.*, 2021, **24**, 31.

57 J. Lee, J. Y. Moon, J. C. Lee, T. I. Hwang, C. H. Park and C. S. Kim, *Carbohydr. Polym.*, 2021, **253**, 117191.

58 A. Rojas, E. Velásquez, C. Piña, M. J. Galotto and C. López de Dicastillo, *Carbohydr. Polym.*, 2021, **261**, 117849.

59 R. Sinha, S. Janaswamy and A. Prasad, *Materialia*, 2020, **14**, 100881.

60 S. Inukai, N. Kurokawa and A. Hotta, *Compos. – A: Appl. Sci. Manuf.*, 2018, **113**, 158.

61 P. K. Szewczyk, D. P. Ura, S. Metwally, J. Knapczyk-Korczak, M. Gajek, M. M. Marzec, A. Bernasik and U. Stachewicz, *Polymers*, 2018, **11**, 34.

62 U. Stachewicz, C. A. Stone, R. Willis, A. H. Barber, C. R. Willis and A. H. Barber, *J. Mater. Chem.*, 2012, **22**, 22935.

63 P. Fei, L. Liao, B. Cheng and J. Song, *Anal. Methods*, 2017, **9**, 6194.

64 D. P. Ura and U. Stachewicz, *Macromol. Mater. Eng.*, 2022, 2100843.

65 S. S. Nair and A. P. Mathew, *Carbohydr. Polym.*, 2017, **175**, 149.

66 R. R. Kalmer, M. Mohammadi, G. Najafpour, M. Golizadeh, Y. Haghighatnia and A. Karimi, *Biointerface Res. Appl. Chem.*, 2020, **10**, 5387.

67 Y. Gu and D. Li, *J. Colloid Interface Sci.*, 2000, **226**, 328.

68 T. Busolo, D. P. Ura, S. K. Kim, M. M. Marzec, A. Bernasik, U. Stachewicz and S. Kar-Narayan, *Nano Energy*, 2019, **57**, 500.

69 D. Zhou, J. Xu, Q. Li, Y. Guan, F. Cao, X. Dong, J. Müller, T. Schenk and U. Schröder, *Appl. Phys. Lett.*, 2013, **103**, 192904.

70 Y. Calahorra, A. Datta, J. Famelton, D. Kam, O. Shoseyov and S. Kar-Narayan, *Nanoscale*, 2018, **10**, 16812.

71 X. Liu, X. Kuang, S. Xu and X. Wang, *Mater. Lett.*, 2017, **191**, 189.

72 J. E. Karbowniczek, Ł. Kaniuk, K. Berniak, A. Gruszczyński and U. Stachewicz, *Front. Bioeng. Biotechnol.*, 2021, **9**, 1.

73 P. K. Szewczyk, S. Metwally, Z. J. Krysiak, Ł. Kaniuk, J. E. Karbowniczek and U. Stachewicz, *Biomed. Mater.*, 2019, **14**, 065006.

74 J. Nicolas, S. Magli, L. Rabbachin, S. Sampaolesi, F. Nicotra and L. Russo, *Biomacromolecules*, 2020, **21**, 1968.

75 H.-Y. Chang, W.-L. Kao, Y.-W. You, Y.-H. Chu, K.-J. Chu, P.-J. Chen, C.-Y. Wu, Y.-H. Lee and J.-J. Shyue, *Colloids Surf., B*, 2016, **141**, 179.

76 S. Metwally, J. E. Karbowniczek, P. K. Szewczyk, M. M. Marzec, A. Gruszczyński, A. Bernasik and U. Stachewicz, *Adv. Mater. Interfaces*, 2019, **6**, 1970010.

77 M. Minary-Jolandan and M. F. Yu, *Appl. Phys. Lett.*, 2010, **97**, 153127.

78 A. J. Bur, *J. Biomech.*, 1976, **9**, 495.

79 P. Vaněk, Z. Kolská, T. Luxbacher, J. A. L. García, M. Lehocký, M. Vandrovcová, L. Bačáková and J. Petzelt, *J. Phys. D: Appl. Phys.*, 2016, **49**, 175403.

80 D. A. Cerqueira, G. Rodrigues Filho and R. M. N. Assunção, *Polym. Bull.*, 2006, **56**, 475.

81 E. Borzabadi, A. S. Vaughan and A. G. Bailey, in *Annual Report Conference on Electrical Insulation and Dielectric Phenomena*, IEEE, 2003, pp. 193–196.

82 S. Jesse, A. P. Baddorf and S. v. Kalinin, *Appl. Phys. Lett.*, 2006, **88**, 062908.